AIAA SciTech Forum
January 3-7, 2022, San Diego, CA & Virtual
AIAA SCITECH 2022 Forum

10.2514/6.2022-1996

Forecasting the Operational Lifetime of Electric Aircraft Through Battery Degradation Modeling

Matthew A. Clarke* and Juan J. Alonso †
Department of Aeronautics and Astronautics, Stanford University, Stanford CA, 94305

In recent years, advancements in high energy and power density batteries have become central to the development of viable aircraft for urban air mobility (UAM). In this paper, we introduce the idea of integrating battery lifetime modeling into the assessment of all-electric aircraft meant to service commuter routes, both within polycentric metropolitan regions and between residential and commercial spaces. Four aircraft that represent the major configuration classes of UAM concepts were simulated under continuous operation spanning a period of one year. The aircraft flew eight daily flights, with recharging of the battery pack occurring at the end of each flight. The behavior of aircraft powertrains presented in this study offers a more holistic perspective on the limitations of battery-powered aircraft than other traditional, non-temporal methods. Results from this study highlight that depending on the vehicle configuration, range and battery pack size, the battery life of achievable missions can fall by as much as 45%. Additionally, findings reveal that the rate of change in an operational lifetime can range between 8-23 days per nautical mile flown. The unearthed findings can equip air transportation network modelers with information critical to improving strategies for optimizing vehicle utility to maximize revenue from such a service.

I. Introduction

Within the aerospace sector, the notion that "time is money" presides over airlines competing to provide affordable and reliable services as well as manufacturers assembling aircraft on the factory floor. Every year, millions of dollars are spent streamlining these processes, which, for airlines, include boarding and deboarding, routine maintenance and inspection. Likewise in the aircraft manufacturing domain, companies strive to accelerate the design-to-certification process of hardware systems and onboard flight software. After all, money is made when aircraft are in the air and not parked on the tarmac.

Such undertakings are not exclusive to the commercial aircraft in service today but apply across the board to newly proposed concepts for long-range supersonic travel and short-range intra-city commuting. This paper is concerned with the latter, and more specifically, the category of aircraft intended for UAM, for which a concerted effort has been made to promote the use of clean technology. This however presents several challenges as the energy and power densities of stored energy cells pale in comparison to what can be achieved through internal combustion using aviation fuel. In response, fast charging and battery swapping have been put forth as potential solutions for reducing idles time between flights. However, despite the belief that the latter, that is, swapping out a fully-discharged battery pack for a charged one can be an option for addressing long charge times between flights, in practice, the repeated removal and insertion of packs can have detrimental and potential hazardous implications such as weakening the structural integrity of the electrical ports on the main airframe. Defective or partially connected packs can lead to scenarios of dangerously high voltages and resistances which may cause permanent damage to the individual cells. Furthermore, combining this with the fact that most aircraft batteries are comprised of several modules located around the airframe for balancing purposes, the chances of a hazard become proportional to the number of independently connected modules. From a ground operations standpoint, this swapping ordeal could even be longer than recharging, as any removal of battery modules around a non-conventional airframe such as an electrical vertical takeoff and landing (EVTOL) aircraft will require skilled labor. Any mishap on the ground can result in delayed service that puts passengers at an inconvenience, or in graver circumstances, fatal incidents in the air. For these reasons, the majority of EVTOL aircraft developers have opted for fixed battery packs that are recharged onboard. Consequently, understanding how the continuous operation and environmental conditions impact battery health becomes crucial for predicting when routine maintenance is required.

*Ph.D. Candidate, Department of Aeronautics and Astronautics, AIAA Student Member
†Professor, Department of Aeronautics and Astronautics, AIAA Fellow

In this paper, we examine electric aircraft operating repeated, identical flights over an extended period of time to gauge market revenue potential of future service providers. The aircraft in this study are powered by battery packs comprising 18650 (jelly-rolled cylindrical structure) lithium nickel manganese cobalt oxide (NMC) cells. In addition to having high specific energy and power densities compared to other lithium-ion cells, these cells have a larger operating window than other electrochemical cells such as lead-acid. They also do not require complex infrastructure for safe operation, which is the case with molten salt cells such as sodium-nickle chloride. Nonetheless, despite being ideal for electric vehicles, the available energy within the battery diminishes with cyclic use as demonstrated in [1–4]. The process by which cells age is divided into mechanisms – calendar aging and cycle aging. The prior is concerned with aging with respect to time while the latter refers to the deterioration of the cell due to repeated charging and discharging. Performance degrades as a result of external environmental conditions such as ambient temperature as well as irreversible physical-chemical changes occurring within the cell. These internal processes include resistive heat dissipation, mechanical stress due to the particle interclation and deinterclation at the electrodes, and the growth of a Solid Electrolyte Interphase (SEI) layer at the graphite anode.

In this study, we employ the comprehensive model developed in previous work [5] for predicting the state of charge (SOC) during cycling as well as the state of health (SOH) over an extended period of use. The remainder of this paper is broken into four sections: Section II is a review of potential routes for UAM in U.S. cities and the market potential of this mode of transportation; Section III provides the geometric and powertrain specifications of the aircraft studied; Section IV outlines additional information about the flight profiles for each vehicle; lastly, Section V presents a compacted representation of findings with the aid of Time-dependent Aircraft Performance Over Operational Lifetime (TAPOOL) diagrams.

II. Urban Air Mobility and Potential Business Cases

UAM has garnered significant traction over the past decade. This can be attributed to an assortment of factors including overburdened and under-maintained infrastructure, the lack of real estate upon which to expand roads and railways, a growing concern over greenhouse gas emissions and the rising passenger dissatisfaction stemming from traffic gridlock. It was therefore not a matter of if, but when will UAM become part of the discussion of future transportation infrastructure within large cities around the world. Thus far, several studies have sought to outline roadmaps for making this a reality. The fraction of them which focus on market valuation has attempted to evaluate potential use cases, determine optimum vertiport location and density, estimate total journey and wait times, quantify cost per seat mile, and forecast the point of net-positive profit among others. In terms of use cases, Booz Allen Hamilton [6] identified three that have been widely accepted as the most promising. These are last-mile delivery of packages from local distribution hubs, air-shuttles resembling other transit options such as buses and subways, with regularly scheduled, predetermined routes and ridesharing air-taxis allowing commuters to request pick-up and drop-off destinations. In this report, they also identified potential cities where the first rollout of UAM operations could occur, four of which are discussed in greater detail in subsequent sections. Another study by Goyal et al. [7] utilized Monte-Carlo simulations to study the scale of UAM operations required to realize an annual market valuation of 2.5 billion U.S. dollars. Of course, this rollout is expected to happen in phases over a period of time, affording market modelers the opportunity to collect consumer data and aircraft manufacturers the opportunity to iterate vehicle design while simultaneously expanding production. Moreover, since the initial cost per mile is expected to be high, the placement of the first vertiports must be done judiciously. In response, some studies have integrated gross domestic product per capita into models predicting market growth [8, 9]. Others such as Robinson et al. [10] have factored in climate, urban density, the number of existing airports, traffic congestion and the presence of various economic clusters into the identification of potential locations for launching operation locations. In fact, one of these candidates, San Francisco, was also suggested by Antcliff et al. [11] to be an early adopter due to the high percentage of long-distance commuting from peripheral cities such as Stockton, Tracy, and San Rafael to name a few.

From a review of these studies, a list of potential routes in four cities is provided in Table 1. Though the majority of nodes are of existing airport listed by their three-letter geocode, there are a few, denoted (*) that are new vertiports. These are Downtown Los Angeles (DLA), Lower Manhattan (LMX), New Brunswick (NBX), Downtown Dallas (DLX), Denton (DDX), McKinney (MDX) and Downtown Fort Worth (FWX). Routes within the table are demarcated as solid lines on Figure 1, while other potential routes between nodes are highlighted with dashed lines. All distances are given in nautical miles (nmi).

Apart from public acceptance, issues concerning aircraft noise, pilot training, the degree of autonomy in the flight controls and the maturity of stored energy systems still linger. These aspects are all closely tracked by investors who are

betting on large returns on their investments. Regulatory agencies are also tracking these technical domains, which, to varying degrees, all have an impact on the built and natural environment. Under the microscope in this study is the operation of lithium-ion batteries subjected to realistic loads over extended periods across select ranges. These ranges reflect the gamut of business cases, from regional flights (70−120 nmi) between closely spaced cities such as San Francisco and Sacramento, mid-range (70−40 nmi) flights between polycentric cities like Dallas-Fort Worth, and short-range flights (10−40 nmi) within cities themselves.

Table 1 UAM destinations in four major metropolitan areas within the U.S.

Metropolitan Area	Route	Range (nmi)
San Francisco Bay Metropolitan Area	SFO - SJC	26
	OAK - SMF	78
	OAK - SJC	26
	PAO - OAK	17
	AFA - SFO	21
	SFO - SCK	56
New York Metropolitan Area	LMX* - JFK	10
	HVN - LGA	55
	EWF - JFK	21
	NBX* - LMX*	26
	HVN - JFK	50
	JFK - ISP	50
Los Angeles Metropolitan Area	LAX - SNA	31
	SBD - SNA	41
	BUR - SBD	53
	DLA* - LAX	10
	SNA - CLD	35
	PMD - LAX	44
Dallas - Fort Worth Metropolitan Area	DLX - DFW	27
	DFW - DLX*	13
	DFW - FWX*	16
	MLX* - DLX*	28
	FWX* - DDX*	37
	MLX* - DDX*	25

III. Electric UAM Aircraft Configurations

The four electric aircraft modeled in this study were an electric conventional takeoff and landing (ECTOL) aircraft, a stopped-rotor EVTOL aircraft, a tandem tilt-wing EVTOL aircraft and hexacopter EVTOL aircraft. Renderings of these vehicles are provided in Figure 2. Their distinct configurations span the four major categories of aircraft envisioned to facilitate UAM. Inspiration for the aircraft was taken from NASA's X-57, Archer's Maker, Airbus's Vahana and the now-retired CityAirbus concept respectively. The ECTOL aircraft is a high-wing airplane with an engine (motor and rotor combination) mounted near the mid-span on each wing. Due to the absence of vertical lift rotors or fans, this aircraft requires takeoff field lengths that are two orders of magnitude greater than EVTOL aircraft, limiting its operation to standard airports with runways. The stopped-rotor on the other hand is of the lift+cruise EVTOL category and is characterized by separate powertrains for vertical climb and forward flight. The transition between hover and cruise is made possible through a combination of these separate propulsive systems. Estimating the electrical load drawn by the motors during transitioning phases of flight is somewhat non-trivial, requiring medium to high fidelity

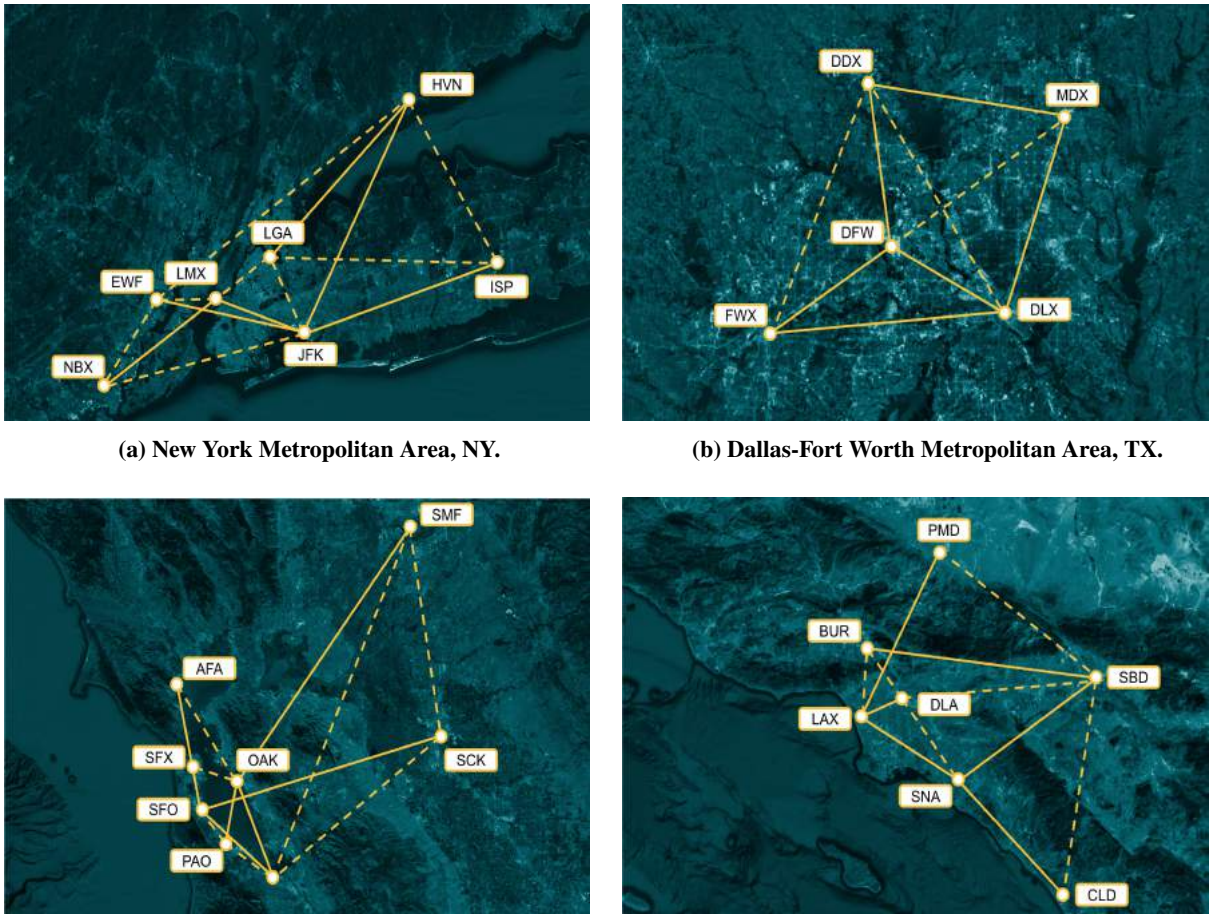

(a) New York Metropolitan Area, NY.

(b) Dallas-Fort Worth Metropolitan Area, TX.

(c) San Francisco Bay Metropolitan Area, CA.

(d) Los Angeles Metropolitan Area, CA.

Fig. 1 Potential UAM routes in four major metropolitan areas within the U.S.

computational methods to accurately predict the forces and moments about the vehicle. Next is the tandem tilt-wing aircraft which is of the vectored-thrust EVTOL type. The particular aircraft in this study possess eight engines, with four mounted on each the front canard and aft main wings. This vehicle uses a combination of lifting surfaces and thrust-vectoring to perform transitioning maneuvers. Lastly, the hexacopter is a six-rotor multi-rotor EVTOL aircraft with engines mounted above the fuselage using struts (not modeled in the image).

Table 2 provides a high-level overview of each aircraft to facilitate the reproduction of findings presented in later sections of this paper. The aircraft are all designed to carry 6 passengers or an equivalent payload of 925 lbs. Other geometric parametrizations were inspired from publicly available information of the reference aircraft. Documented in Clarke and Alonso [5] are the semi-empirical models that capture the impact of continuous cycling and environmental conditions. As the modules of the battery pack are assumed to be air-cooled, a model of the ambient temperature is required. This was obtained from the National Centers for Environmental Information [12] for the San Francisco Bay metropolitan area. Within the modules, flow conditions are dominated by boundary-layer separation effects and wake interactions. There were therefore modeled as tube banks in a crossflow using empirical correlations outlined in Bergman et. al [13] to estimate the heat removed from the system. The size and breakdown of battery packs are also documented in Table 2. Here, ($\parallel$) represents the number of cells parallel to the cooling airflow and ($\perp$) represents the number of cells perpendicular to the cooling airflow with a module. The spacing between cells was set to 2 mm for all modules. The electrical circuit layout at both the module and pack levels is also provided in the table below. Here, "s" denotes the number of units (cells or modules) in series and "p" denotes the number of units in parallel. Lastly, SOH is assumed to be uniform across all cells in the battery pack. This of course is not the case in real life as even with the aid of state-of-the-art quality control, pristine cells can vary ever so slightly. One of the functions of battery management

systems (BMS) is therefore to balance during discharging and charging to ensure that no one cell experiences electrical loads beyond its manufacturer-rated limits. Powertrains of the aircraft were sized based on design loads computed through a physics-based component weight build-up approach by Smart [14]. This ensured that the aerodynamic and propulsion network analysis routines captured realistic estimates of flight load and energy consumption. A detailed description of vehicle sizing and the weight breakdown can be found in previous work by Clarke and Alonso [15].

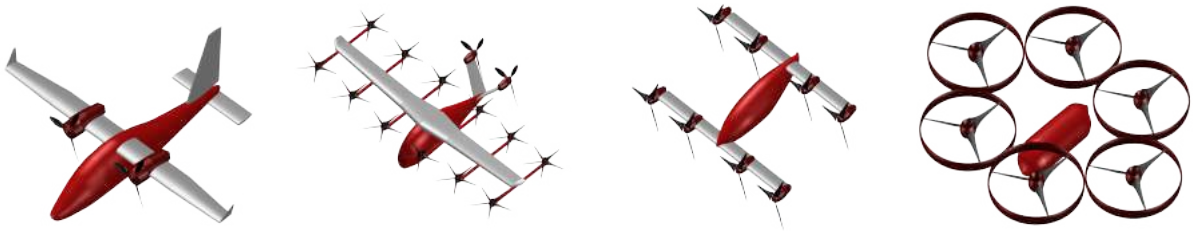

(a) Twin-engine ECTOL. **(b) Stopped-rotor.** **(c) Tandem tilt-wing.** **(d) Hexacopter.**

Fig. 2 Electric aircraft models.

Table 2 Vehicle parameters.

	ECTOL	Stopped-rotor	Tandem Tilt-wing	Hexacopter
		General Vehicle Characteristics		
Capacity (pass.)	6	6	6	6
Radial Footprint (ft)	36	48	32	39
Reference Area (ft^2)	159	180	234	96
TOGW (lbs)	3947	6113	6007	8381
Battery				
Pack Capacity (kW-hr)	92	179	249	631
Number of Modules	10	10	10	10
Module Geometric Layout	12 $\parallel \times 6 \perp$	14 $\parallel \times 10 \perp$	15 $\parallel \times 13 \perp$	19 $\parallel \times 26 \perp$
Module Electrical Layout	12s × 60p	14s × 100p	15s × 130p	19s × 260p
Pack Electrical Layout	10s × 1p	10s × 1p	10s × 1p	10s × 1p
Powerplant				
Rotors	2 propellers	2 propellers 12 rotors	8 rotors	6 rotors
Motors	2 × 83 kW motors	2 × 221 kW motors 12 × 47 kW motors	8 × 108 kW motors	6 × 155 kW motors
Propeller Diameter (ft)	6.3	7.5	-	-
Rotor Diameter (ft)	-	7.5	7.9	16.4
		Performance		
Cruise Speed (mph)	175	175	175	75
Maximum Operational Altitude (ft)	14000	5000	5000	2500

IV. Operational Lifetime Simulations

The open-source, python-based code, SUAVE [16] is used to perform simulations. This platform was developed with modularity in mind, allowing design freedom in the propulsion network model as well as the choice in the level of fidelity for analyzing both component-level and full configuration performance. At each pseudo-spectral collocation point, both dimensional quantities and non-dimensional coefficients are computed by the mission-solver. In previous work [17], we demonstrated the importance of modeling the flight mechanics of all segments that define an aircraft's trajectory. For example, during climb to cruising altitudes, non-linear throttle profiles arise even in constant-speed fight segments by virtue of the aircraft flying through a varying density atmosphere. Instantaneous C-rate also exhibits non-linear behavior in constant power segments as the remaining energy in the battery depletes over time. This quantity paints a clearer picture of battery cycle life than the more commonly used nominal C-rate, which by definition refers to the rate of discharge relative to a cell's nominal capacity. Instantaneous C-rate on the other hand is a measure of the cell's ability, at its current SOC, to supply the energy required by the motors. This observability becomes increasingly important near the end of the cycle where the cell reaches the knee point on the SOC curve and any loads past this point will see a drastic drop in performance.

The flight profile of each aircraft is detailed in Table 3 with a more descriptive summary of rigid body kinematics is provided in Table 4. The specific values used in the simulation of each flight profile, including altitude, speed, climb rate, rotor orientation angle and pitch command for each segment, are also provided in Table 6 in the Appendix. These rotor orientation angles are given relative to the body axis of the aircraft, with the $+ve$ x-axis pointing out the nose of the aircraft. For example, a rotor angle of [0°, 90°, 0°] indicates a rotation about the $+ve$ y-axis pointing out the starboard wing by 90°. The axis about where the rotor blades revolve in such a case is therefore now aligned with the $+ve$ z-axis of the vehicle. For brevity in Table 6, only the rotations about the $+ve$ y-axis rotation are provided as no orientations out of the vehicle's x-z plane were modeled. Additionally, the blade pitch command listed in this table can be thought of as the additional angle uniformly added to each blade section in the Blade Element Momentum Theory analysis subroutine of SUAVE's energy analysis. For the stopped-rotor EVTOL aircraft, the first value in both the rotor orientation and blade pitch command columns correspond to the propeller (forward flight) while the second column corresponds to the lift-rotor (vertical flight). For the tandem tilt-wing EVTOL aircraft, the incidence angles of both the rear main wing and the lower forward tandem wing are equivalent to rotor orientation angles throughout the mission and were not repeated. A comparison of the aerodynamic, acoustic and powertrain performances of these for aircraft flying their respective flight profiles is documented in Clarke and Alonso [15] and thus the authors choose to refer readers to this study.

Table 3 Aircraft flight segments.

Segment	Twin-engine ECTOL	Stopped-rotor	Tilt-wing	Hexacopter
1	Take-off	Vertical Climb	Vertical Climb	Vertical Climb
2	Departure End of Runway	Vertical Transition	Vertical Transition	Vertical Transition
3	Initial Climb Area	Climb Transition	Climb Transition 1	Climb
4	Climb	Climb 1	Climb Transition 2	Cruise
5	Cruise	Climb 2	Climb	Descent
6	Descent	Cruise	Cruise	Descent Transition
7	Downleg	Descent	Descent	Vertical Descent
8	Baseleg	Approach Transition	Approach Transition	
9	Final Approach	Descent Transition	Descent Transition	
10	Landing	Vertical Descent	Vertical Descent	

Detailed in Table 5 are the nine ranges each aircraft is simulated through, all processing similar climb and descent segments – only the cruise segment is modified. As can be seen in the table, the distances of hexacopter ranges are well below that of the other three aircraft, underscoring this vehicle's inability to perform long-range flight operations. This is due to the large amounts of power required by this configuration to perform cruises without the benefit of wings that enable efficient long-range flight. Lastly, the eight daily flights reflect the continuous services that UAM businesses are expected to operate. Recharging at 1C from the end-of-flight SOC to 100% SOC was also simulated after each flight. This of course does not necessarily mean that the battery reaches the same capacity as its pristine state since the cell ages with time.

Table 4 Flight segment kinematics in SUAVE.

Segment	Symbol	Segment Kinematics
Approach Transition	AT	Constant-Acceleration-Constant-Angle-Linear-Climb
Baseleg	BL	Linear-Speed-Constant-Rate
Climb	CL	Linear-Speed-Constant-Rate
Climb Transition	CT	Constant-Acceleration-Constant-Angle-Linear-Climb
Cruise	CR	Constant-Speed-Constant-Altitude
Departure End of Runway	DER	Linear-Speed-Constant-Rate
Descent	D	Linear-Speed-Constant-Rate
Descent Transition	DT	Constant-Acceleration-Constant-Pitchrate-Constant-Altitude
Downleg	DL	Constant-Acceleration-Constant-Altitude
Final Approach	FA	Linear-Speed-Constant-Rate
Initial Climb Area	ICA	Linear-Speed-Constant-Rate
Vertical Climb	VC	Vertical Ascent
Vertical Transition	VT	Constant-Acceleration-Constant-Pitchrate-Constant-Altitude
Vertical Descent	VD	Vertical Descent

Table 5 Simulated ranges of the electric aircraft.

	Range (nmi)								
Aircraft	**Case 1**	**Case 2**	**Case 3**	**Case 4**	**Case 5**	**Case 6**	**Case 7**	**Case 8**	**Case 9**
Twin-engine ECTOL	60	65	70	75	80	85	90	95	100
Stopped-rotor EVTOL	60	65	70	75	80	85	90	95	100
Tilt-wing EVTOL	60	65	70	75	80	85	90	95	100
Hexacopter EVTOL	20	22.5	25	27.5	30	32.5	35	37.5	40

V. Time-dependent Aircraft Performance Over Operational Lifetime (TAPOOL) Diagrams

Simulating extended periods of time presents two unique challenges: representing large amounts of information and determining how best to weigh the various aspects of vehicle performance. On top of this, with the incorporation of temperature as a function of both altitude and time of year, some observations exhibit strong bi-variance. We therefore rely on TAPOOL diagrams as a means of describing the behavior of an electric aircraft's battery pack under realistic flight and environmental conditions. This differs from traditional approaches of assessing battery-powered aircraft [18] in two ways: 1) time-dependency is introduced into the efficiency criteria of stored-energy systems and 2) the full flight profile which includes the climb and descent stages of a mission is used rather than simply assuming constant altitude and speed in the computation of range and endurance.

The performance of the battery in any given flight segment is also directly affected by its history or rather the electrical load that pack is subjected to during the previous segment. This meant that simulations had to be performed in sequence and computational operations could not be parallelized. Depending on the aircraft configuration, simulations therefore took between 2-5 days on a single node on the in-house 8-node cluster of the Aerospace Design Lab at Stanford University. Hence, the data presented in the study was amassed over a period of one month. This however is still significantly shorter than running capacity tests on cells within a laboratory setting on a programmable cycler. By and large, there is potential for computer simulations to fill the gaps of experimental data, accelerate testing by addressing the information entropy problem i.e. determining is the least amount of information required to fully characterize cell aging, and predict battery end-of-life. The following subsections discuss the TAPOOL diagrams for battery cell capacity, ohmic resistance, maximum cell temperature and maximum instantaneous C-rate. These four variables were deemed to be the most significant given their implications on both safety and performance at the systems level. In the figures below, simulations are terminated when the SOC at the end of a flight first reaches a lower threshold of 20%, signifying the end of useful life. The decision to use this cut-off value over other thresholds of 15% and even 10% suggested by German et

al. [19] was due to the fact that as the cell degrades, the inflection point where there is a precipitous drop in voltage becomes increasingly difficult the predict in practice. The higher cut-off SOC therefore ensures that the simulated operations will be guaranteed. Infeasible regions of flight missions are hashed in back and white on the figures.

A. Battery Capacity

Arguably the most important metric in cell state of health, capacity fade is a measure of the change in the cell's charge storing potential relative to its pristine condition at the beginning of use. This degradation can be credited to several internal mechanisms including the deterioration of the rock salt structure of the cathode, exfoliation of the graphite structure at the anode resulting in a weakening of bonding potential, and the growth of the SEI layer that consumes active material. Figure 3 depicts the behavior of capacity fade as a function of range and number of days in operation. As expected, the general trend across configurations is that longer missions accelerate cell degradation and reduce the operational lifetime. In other words, the number of days that a particular aircraft can fly a given route decreases with increasing cruise distance. For the flight schedules defined in the previous section, it was observed that battery life of achievable missions can drop by as much as 45% by the end of a calendar year depending on vehicle configuration, range and battery pack size, while the rate of change in operational lifetime can range between 8-23 days per nautical mile flown. From a purely utilitarian standpoint, the ECTOL aircraft, with the highest operational periods across all ranges, is the most energy efficient option. This however does not factor in the footprint needed for takeoff by such a configuration, which poses a significant dilemma for operating in urban spaces. Taking a step back to assess the implications of these trends on vehicle choice, we see from a graphical analysis that the lifetime of operation of the ECTOL, stopped-rotor EVTOL, tilt-wing EVTOL and hexacopter EVTOL aircraft decreases by 11, 8, 9 and 23 days

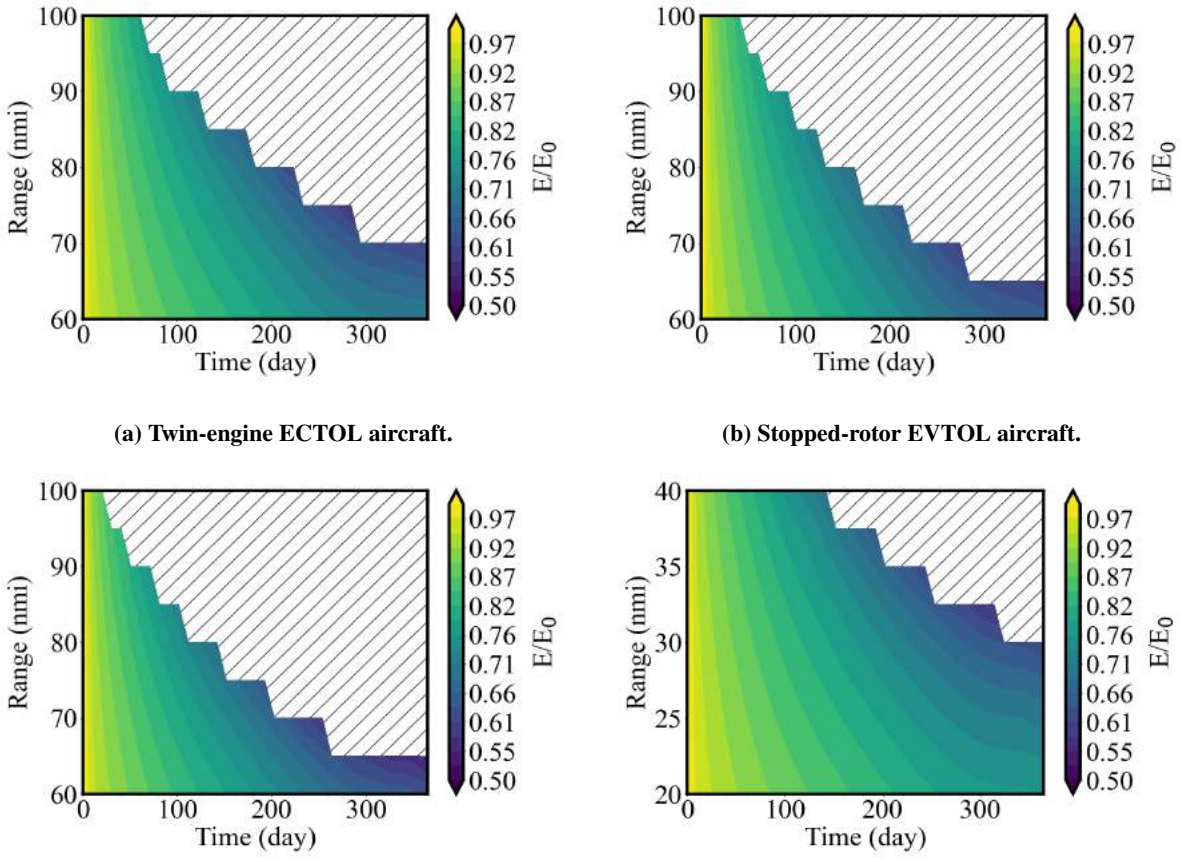

(a) Twin-engine ECTOL aircraft.

(b) Stopped-rotor EVTOL aircraft.

(c) Tiltwing EVTOL aircraft.

(d) Hexacopter EVTOL aircraft.

Fig. 3 Cell capacity TAPOOL contours.

respectively for every additional nautical mile flown. These linearized approximations were computed by examining end-of-life states at the 90 and 70 nmi ranges for the first three vehicles and 37.5 and 30 nmi for the hexacopter. It is important to note that these rates are not necessarily a comparison of energy consumption in the respective battery packs but rather the rate at which this energy depletes. These rates do however provide direction to more appropriately size battery packs. The above plots also lend key insights into what strategies air-shuttle and air-taxi services should adopt to maximize the potential of both brand-new and used aircraft. Taking San Francisco for example, we can infer from Figure 3a that a service using a new twin-engine ECTOL aircraft between Oakland International Airport (OAK) and Sacramento International Airport (SMF) will last around 200 days. As another example using Figure 3d, we can arrive at a service period of 350 days for hexacopter operating non-stop between Norman Y. Mineta San Jose International Airport (SJC) and either OAK or San Francisco International Airport (SFO), which are roughly the same distance apart. On the other hand, if we have a tilt-wing EVTOL that has been providing a 90-nmi regional service in the New-York Metropolitan Area between Philadelphia International Airport (PHL) (not shown in Figure 1a) and Lower Manhattan (LMX) for 100 days, it can be repurposed for flights between John F. Kennedy International Airport (JFK) and Long Island MacArthur Airport (ISP) to extend of service life by another 200 days before battery pack replacement is needed.

B. Battery Ohmic Resistance

The magnitude of resistance within a battery cell is predominantly dictated by the thickness of the SEI layer which, among other things, acts as a passivating agent in the binding of free lithium ions in the layered graphite structure of the anode. In contrast to the capacity fade of the NMC cell, there is nearly a 300% increase in resistance over a year. These observations not only highlight that the cell undergoes a decrease in energy storage capacity over time but a drop in

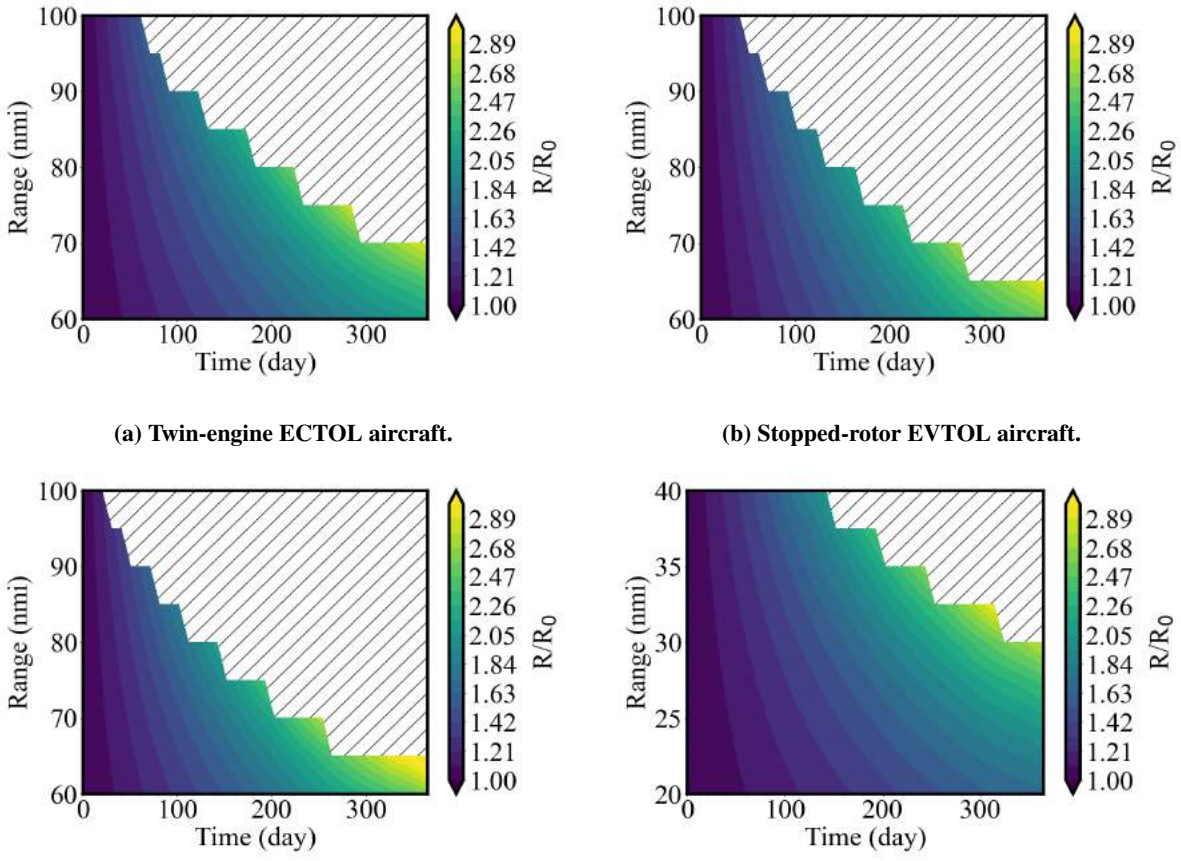

(a) Twin-engine ECTOL aircraft.

(b) Stopped-rotor EVTOL aircraft.

(c) Tiltwing EVTOL aircraft.

(d) Hexacopter EVTOL aircraft.

Fig. 4 Ohmic resistance TAPOOL contours.

efficiency of power conversion from the electrochemical cell to the electromechanical components, notably the electric motors.

C. Maximum Instantaneous C-Rate

Shown in Figure 5 are the changes in current severity passing through a particular cell at any given instant in time. Before we elaborate on these trends, it is important to first remind readers of the terminology concerning C-rate used in this study. Continuing the discussion in Section IV, nominal C-rate can be viewed as the current through the battery divided by the current draw under which the battery would deliver its rated capacity in one hour. For example, a discharge of 2-C of a 1Ah cell indicates that the cell would be fully-discharged in 30 minutes. This rated capacity is typically provided by the manufacturer but can be experimentally determined in the lab [20]. In contrast, we utilize instantaneous C-rate, defined here as the rate at which a battery is discharged relative to its current capacity. This was the preferred metric as it allows us to understand the differences between discharges of equivalent magnitude at opposite ends of the SOC range, that is, fully-charged and fully-discharged. Instantaneous C-rate conveys how severe discharges near the end-of-cycle are to battery health.

As the battery ages and the voltage as a function of SOC drops, more current is required to supply the same power to the powertrain. The maximum C-rate for the four aircraft therefore all increase with increasing range and length of operation. We can also deduce from Figure 5c that despite the battery pack of the tilt-wing EVTOL aircraft being sized to meet mission specifications at the beginning of service, the electrical layout (number of cells in series and parallel) was not copiously done, resulting in extremely high C-rates as time progresses. This observation would not have been observed in a single-flight analysis, and further demonstrate the versatility of TAPOOL diagrams.

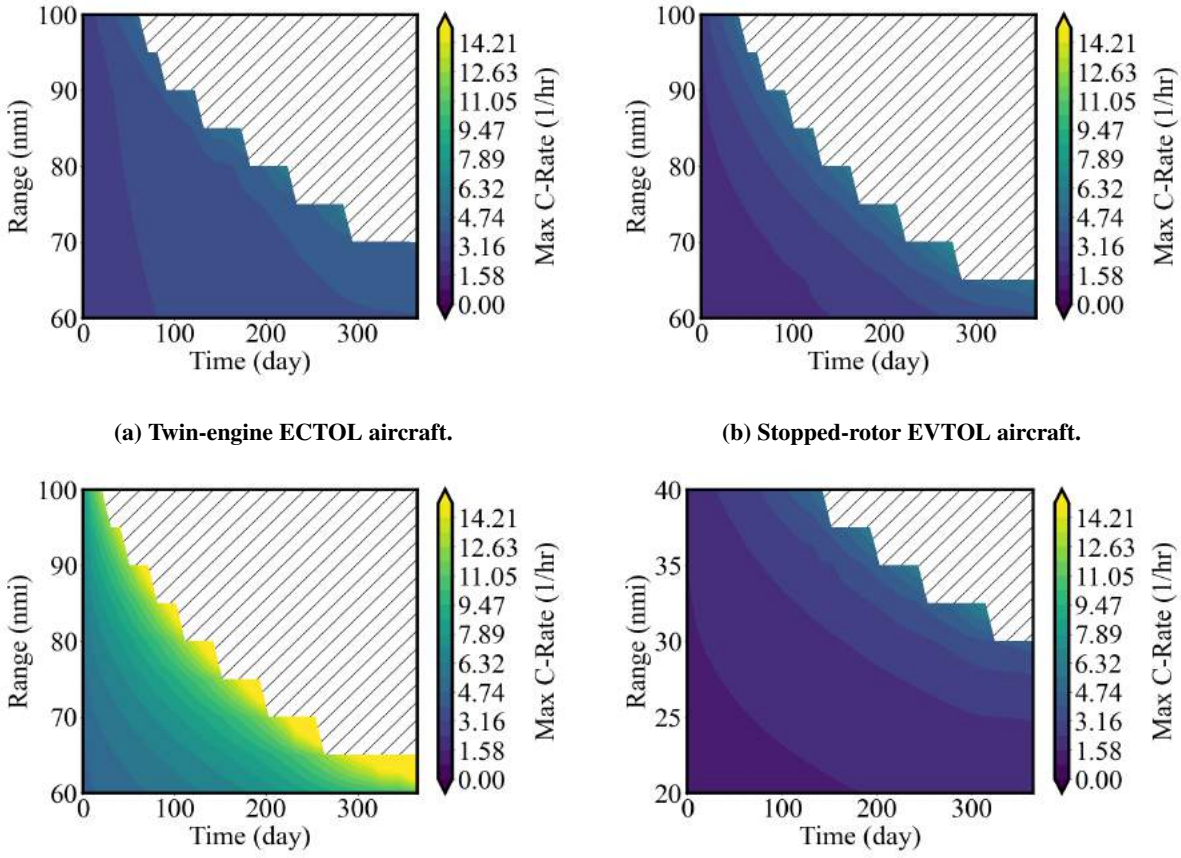

(a) Twin-engine ECTOL aircraft.

(b) Stopped-rotor EVTOL aircraft.

(c) Tiltwing EVTOL aircraft.

(d) Hexacopter EVTOL aircraft.

Fig. 5 Maximum instantaneous C-rate TAPOOL contours.

D. Maximum Cell Temperature

Accompanying the increase in ohmic resistance within the battery cell is is the increase in temperature. Cell temperature mirrors the last two measured quantities discussed above, however, this trend exhibits strong bi-variance and is somewhat offset by the ambient temperature which changes year-round. For example, if we examine a 65 nmi mission of the twin-engine ECTOL aircraft in Figure 6a, we gather that during the months of August and September, the temperature within the battery module can reach around 318 K or 45 °C. In longer-range missions, temperatures can even reach 324 K or 50 °C earlier in the year as a result of a rise in accumulated heat energy during cruise segments of the flight profile. This temperature increase is the direct result of the constant airflow of the cooling air in the simulations which governs heat rejection.

Generally speaking, all electrochemical cells have an optimum temperature range of operation, lithium-ion battery cells included. Operating within this window not only guarantees that the battery can perform at its full potential, but prolongs the life of the cell. The temperature TAPOOL diagram hence provides system designers with critical insights into the design of the thermal management system and the cell layout needed to achieve ideal operating conditions within the module.

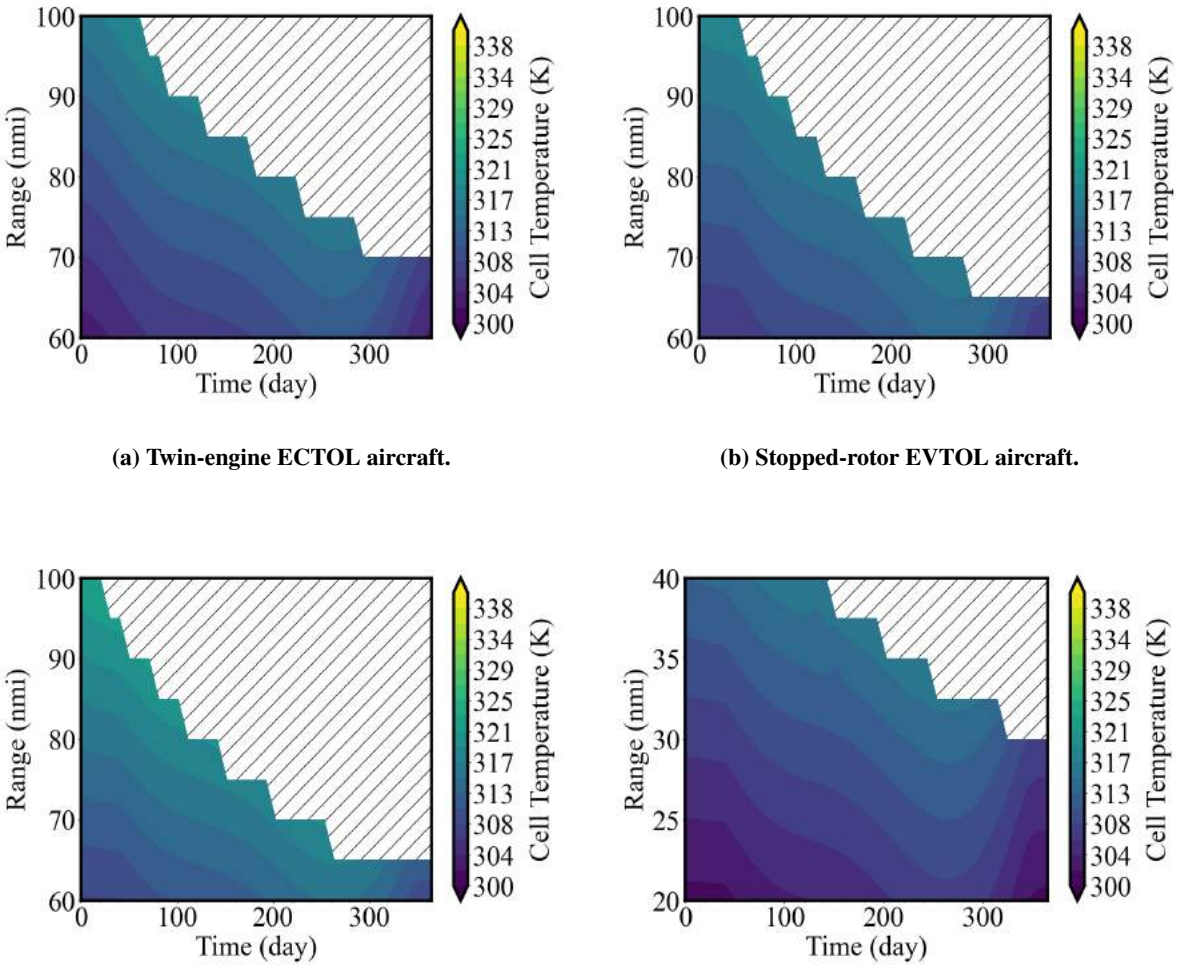

(a) Twin-engine ECTOL aircraft.

(b) Stopped-rotor EVTOL aircraft.

(c) Tiltwing EVTOL aircraft.

(d) Hexacopter EVTOL aircraft.

Fig. 6 Maxiumum temperature TAPOOL contours.

VI. Conclusions

Any comprehensive assessment of the performance of stored energy systems such as battery-power aircraft must involve the incorporation of time-dependent factors that capture the reduction in efficiency with repeated use. This paper demonstrates the application of lithium-ion degradation models to studying aircraft performance, specifically flight operations symbolizing regional and urban air mobility commuting. The findings of this study suggest that after a year of continuous operation, albeit excessive in terms of the number of flights per day, can lead to a reduction in battery capacity by as much as 45%. Results from the simulated campaigns also highlight potential areas of exploration in lithium-ion battery development, including the cell-level areas such as engineering of cells tailored for aerospace applications, that is, high C-rate discharge during the beginning and end of cycle life. This process is referred to as battery inverse-design. Other domains at the module level developing more robust thermal management system algorithms given that we can now predict thermal loads. Finally, at the systems level, the findings of this study present the opportunity to conceptualize flight operation strategies to maximize vehicle life before significant ground maintenance is needed.

References

[1] Zhang, C., Yan, F., Du, C., Kang, J., and Turkson, R. F., "Evaluating the degradation mechanism and state of health of LiFePO4 lithium-ion batteries in real-world plug-in hybrid electric vehicles application for different ageing paths," *Energies*, Vol. 10, No. 1, 2017. doi:10.3390/en10010110, URL www.mdpi.com/journal/energies.

[2] Cordoba-Arenas, A., Onori, S., Guezennec, Y., and Rizzoni, G., "Capacity and power fade cycle-life model for plug-in hybrid electric vehicle lithium-ion battery cells containing blended spinel and layered-oxide positive electrodes," *Journal of Power Sources*, Vol. 278, 2015, pp. 473–483. doi:10.1016/j.jpowsour.2014.12.047.

[3] Han, X., Ouyang, M., Lu, L., Li, J., Zheng, Y., and Li, Z., "A comparative study of commercial lithium ion battery cycle life in electrical vehicle: Aging mechanism identification," *Journal of Power Sources*, Vol. 251, 2014, pp. 38–54. doi:10.1016/j.jpowsour.2013.11.029, URL http://dx.doi.org/10.1016/j.jpowsour.2013.11.029.

[4] Yan, D., Lu, L., Li, Z., Feng, X., Ouyang, M., and Jiang, F., "Durability comparison of four different types of high-power batteries in HEV and their degradation mechanism analysis," *Applied Energy*, Vol. 179, 2016, pp. 1123–1130. doi:10.1016/j.apenergy.2016.07.054, URL http://dx.doi.org/10.1016/j.apenergy.2016.07.054.

[5] Clarke, M., and Alonso, J. J., "Lithium–Ion Battery Modeling for Aerospace Applications," *Journal of Aircraft*, 2021, pp. 1–13.

[6] Reiche, C., Goyal, R., Cohen, A., Serrao, J., Kimmel, S., Fernando, C., and Shaheen, S., "Urban air mobility market study," 2018, pp. 1–163. URL https://ntrs.nasa.gov/citations/20190001472, [Retrieved 14 Nov. 2021].

[7] Goyal, R., Reiche, C., Fernando, C., and Cohen, A., "Advanced Air Mobility: Demand Analysis and Market Potential of the Airport Shuttle and Air Taxi Markets," *Sustainability*, Vol. 13, No. 13, 2021, p. 7421.

[8] Herman, E., and Dyment, M., "Urban Air Mobility-Economics and Global Markets," Tech. rep., 2018. URL https://www.nexaadvisors.com/uam-global-markets-study, [Retrieved 14 Nov. 2021].

[9] Major, T., and Anderson, J., "Getting Mobility Off the Ground;," Tech. rep., 2019. URL https://institutes.kpmg.us/content/dam/advisory/en/pdfs/2019/urban-air-mobility.pdf, [Retrieved 18 Nov. 2021].

[10] Robinson, J. N., Sokollek, M.-D. R., Justin, C. Y., and Mavris, D. N., "Development of a methodology for parametric analysis of STOL airpark geo-density," *2018 Aviation Technology, Integration, and Operations Conference*, 2018, p. 3054.

[11] Antcliff, K. R., Moore, M. D., and Goodrich, K. H., "Silicon valley as an early adopter for on-demand civil VTOL operations," *16th AIAA Aviation Technology, Integration, and Operations Conference*, 2016, p. 3466.

[12] National Centers for Environmental Information, "Daily Summaries Location Details," , 2019. URL https://www.ncdc.noaa.gov/cdo-web/datasets/GHCND/locations/CITY:US060031/detail, [Retrieved 02 Nov. 2019].

[13] Bergman, T. L., Incropera, F. P., DeWitt, D. P., and Lavine, A. S., *Fundamentals of heat and mass transfer*, John Wiley & Sons, 2011.

[14] Smart, J. T., and Alonso, J. J., "Primary Weight Estimation for eVTOLs via Explicit Analysis and Surrogate Regression," , No. June, 2019, pp. 1–12. doi:10.2514/6.2019-3679.

[15] Clarke, M. A., and Alonso, J., "Evaluating the Performance and Acoustic Footprint of Aircraft for Regional and Urban Air Mobility," *AIAA Aviation 2021 Forum*, 2021, p. 3205.

[16] Botero, E., Clarke, M., Erhard, R., Smart, J., MacDonald, T., Vegh, J. M., Lukaczyk, T., da Silva, C. R. I., Momose, T., Blaufaux, A., Orra, T., and Wendorff, A., "SUAVE 2.5.0," 2021. doi:10.5281/zenodo.5661107, URL https://doi.org/10.5281/zenodo.5661107.

[17] Clarke, M., Smart, J., Botero, E., Maier, W., and Alonso, J., "Strategies for posing a well-defined problem for urban air mobility vehicles," *AIAA Scitech 2019 Forum*, 2019. doi:10.2514/6.2019-0818.

[18] Traub, L. W., "Range and endurance estimates for battery-powered aircraft," *Journal of Aircraft*, Vol. 48, No. 2, 2011, pp. 703–707.

[19] German, B., Daskilewicz, M., Hamilton, T. K., and Warren, M. M., "Cargo Delivery in by Passenger eVTOL Aircraft: A Case Study in the San Francisco Bay Area," *2018 AIAA Aerospace Sciences Meeting*, 2018. doi:10.2514/6.2018-2006, URL https://arc.aiaa.org/doi/pdf/10.2514/6.2018-2006https://arc.aiaa.org/doi/10.2514/6.2018-2006.

[20] Christophersen, J. P., "Battery Test Manual For Electric Vehicles, Revision 3," Tech. rep., Idaho National Lab.(INL), Idaho Falls, ID (United States), 2015.

VII. Appendix

Table 6 Altitude, airspeed and climb rates of UAM aircraft missions.

Flight Segment	Initial Altitude (ft)	Final Altitude (ft)	Initial Speed (mph)	Final Speed (mph)	Climb Rate (ft/min)	Rotor Orient. Angle (deg.)	Blade Pitch Command (deg.)
ECTOL Aircraft							
DER	0	50	111	122	600	0	0
ICA	50	500	122	133	600	0	0
CL	500	2500	133	175	500	0	0
CR	2500	2500	175	175	0	0	0
D	2500	1000	175	144	-300	0	0
DL	1000	1000	144	133	0	0	0
BL	1000	500	133	122	-300	0	0
FA	500	0	122	111	-300	0	0
Stopped-rotor EVTOL Aircraft							
VC	100	140	0	5.6	500	0 , 90	0 , 0
VT	140	140	5.6	87	0	0 , 90	0 , 0
CT	140	100	87	95	*	0 , 90	0 , 0
CL No.1	200	300	95	160	200	0 , 90	0 , 0
CL No.2	400	2500	160	175	500	0 , 90	0 , 0
CR	2500	2500	175	175	0	0 , 90	0 , 0
D	2500	300	175	120	-300	0 , 90	2 , 0
AT	200	140	120	103	*	0 , 90	0 , 0
DT	140	140	103	3.4	0	0 , 90	0 , 0
VD	140	100	3.4	0	-300	0 , 90	0 , 0
Tandem tilt-rotor EVTOL Aircraft							
VC	100	140	0	3.4	300	90	-5
VT	140	140	3.4	55	0	45	3
CT No.1	140	200	55	85	500	15	5
CT No.2	200	200	85	125	0	15	20
CL	200	2500	125	175	500	0	16
CR	2500	2500	175	175	0	0	16
D	2500	200	175	100	-300	0	16
AT	200	140	100	55	-200	15	15
DT	140	140	55	3.4	*	25	5
VD	140	100	3.4	0	-300	90	-5
Hexacopter EVOL aircraft							
VC	100	140	0	3.4	300	90	0
VT	140	140	3.4	35	0	90	3
CL	140	2500	35	75	500	90	2
CR	2500	2500	75	75	0	90	5
D	2500	100	75	35	-200	90	5
DT	140	140	35	3.4	*	90	3
VD	140	100	3.4	0	-300	90	0